International Journal of Microwave and Wireless Technologies

cambridge.org/mrf

A low-cost millimeter-wave collinear slot phased array enabled by ridge-bent RSIW with high inter-element isolation

Sha Xu[1], Wanbin Yang[1], Dujiao Lu[2] and Guiping Jin[2]

[1]School of Integrated Circuits, Guangdong University of Technology, Guangzhou, China and [2]School of Electronic and Information Engineering, South China University of Technology, Guangzhou, China

Research Paper

Cite this article: Xu S, Yang W, Lu D, Jin G (2026) A low-cost millimeter-wave collinear slot phased array enabled by ridge-bent RSIW with high inter-element isolation. *International Journal of Microwave and Wireless Technologies* **18**(5), 731–742. https://doi.org/10.1017/S1759078726103183

Received: 20 September 2025
Revised: 6 April 2026
Accepted: 13 April 2026
First published online: 28 July 2026

Keywords:
5G millimeter-wave (mmWave); collinear slot; high isolation; phased array antenna; ridge substrate integrated waveguide (RSIW)

Corresponding author: Guiping Jin;
Email: gpjin@scut.edu.cn

Abstract

This paper presents a low-cost, high-gain 1 × 4 collinear slot phased array for 5G millimeter-wave (mmWave) applications, which is realized on a two-layer standard printed circuit board. The design specifically addresses two key challenges in mmWave phased array design, which are mitigating the strong mutual coupling that limits wide-angle scanning performance and enabling the low cross-polarization radiation structure. A key innovation is the use of a periodically bent ridge within a ridge substrate integrated waveguide to efficiently excite a centerline collinear slot configuration, which minimizes cross-polarization. Furthermore, a compact via-based choke structure is introduced to suppress mutual coupling and thus achieve high inter-element isolation. The fabricated prototype exhibits an impedance bandwidth of 10.7% (26.5–29.5 GHz). The measured results show a peak gain of 14.5 dBi, port isolation better than 19 dB, and a stable 3-dB scanning range of ±50°. These results validate the proposed design as a compelling low-cost solution that achieves an excellent balance of high gain, wide-angle scanning, and high isolation.

Introduction

The evolution toward 5G and future 6G communication systems has driven significant research into the millimeter-wave (mmWave) spectrum, which offers a broad bandwidth to support high-data-rate services [1–3]. Phased array antennas, which possess beamforming capabilities, are an established and indispensable technology for overcoming the high path loss associated with mmWave frequencies [4–6].

However, the beam-scanning capability of phased arrays is still fundamentally hindered by the limited beamwidth of individual elements and the strong mutual coupling between them [7, 8]. This coupling effect is exacerbated at wide scan angles, causing significant performance degradation [9, 10]. To address these limitations, extensive research has focused on enhancing the scanning range of phased arrays through various strategies, including the use of wide-beam elements [11, 12], the integration of decoupling structures [13, 14], and the reduction of element spacing [15]. Nonetheless, achieving the demanding goal of ±50° wide-angle scanning in a compact and cost-effective configuration continues to be a key research challenge [16].

The ridge substrate integrated waveguide (RSIW) has emerged as a highly suitable platform for wide-angle scanning phased arrays. Compared with substrate integrated waveguide (SIW), it combines the benefits of both ridge waveguides and SIWs, such as a lower cutoff frequency, a broader single-mode bandwidth, and a more compact size [17–19]. This compactness is particularly advantageous for array design, as it facilitates better control over element spacing and sidelobe levels. Moreover, the compact element size provides valuable physical space for integrating decoupling structures to suppress mutual coupling [20]. Furthermore, RSIW is more cost-effective than traditional waveguides and can be seamlessly integrated with planar circuits, such as printed circuit boards (PCBs).

Despite these advantages, realizing high-performance RSIW phased arrays with wide-angle scanning capability remains a challenging task that has not been fully addressed. A review of state-of-the-art methods indicates that many RSIW scanning arrays are based on the leaky-wave antenna (LWA) principle. Mallahzadeh and Mohammad-Ali-Nezhad [21] presented a collinear slot antenna based on a double-ridged SIW. Although it achieves a peak gain of 11 dBi over a ±28° scan range, its beam direction is frequency dependent, which is a characteristic limitation of LWAs. An alternative approach is demonstrated in Wei et al. [22], which employs p-i-n diodes to reconfigure the radiating slots for fixed-frequency scanning. While this method expands the scanning range to ±52°, it comes at the cost of a significant 4.5 dB

© The Author(s), 2026. Published by Cambridge University Press in association with The European Microwave Association.

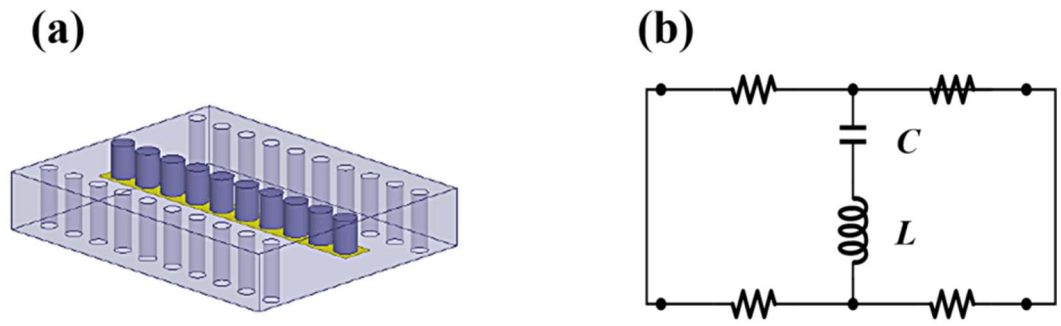


Figure 1. RSIW equivalent circuit model.

gain degradation at the scan edges. The limitations of both frequency-scanned and phase-tuned LWA topologies motivate the investigation of an RSIW phased array capable of delivering wide-angle scanning capabilities without compromising other critical performance metrics.

Different from previously published RSIW scanning arrays, a centerline collinear slot phased array is proposed in this paper. By periodically bending the RSIW ridge, a strong longitudinal current is induced along the RSIW centerline, thereby efficiently exciting the collinear slots for in-phase radiation. This centered arrangement preserves the overall structural symmetry, which is critical for suppressing cross-polarization. To address the challenge of mutual coupling, a via-based choke structure is also strategically integrated between the array elements to enhance isolation. On the basis of this method, a 1 × 4 linear array prototype operating in the n257 band was designed, fabricated, and measured. The experimental results demonstrate that the array achieves a wide impedance bandwidth of 10.7% (26.5–29.5 GHz), a high peak gain of 14.5 dBi, excellent inter-element isolation better than 19 dB, and a 3-dB beam scanning range exceeding ±50°. The proposed design presents an effective solution that combines wide-angle scanning capability with superior gain and isolation performance, making it a compelling candidate for 5G and future mmWave communication systems.

Design of a collinear slot phased array

Working principles of the RSIW with a bending ridge

The fundamental behavior of the RSIW, particularly its cutoff frequency, can be effectively understood using a resonance model. In this approach, the cross-section of the waveguide is modeled as a resonant circuit, as depicted in the transmission line model in Fig. 1.

The central ridge structure, formed by a row of metallic vias, introduces significant capacitive and inductive loading. An equivalent capacitance (C) is formed between the central vias of the ridge and the bottom ground plane. The vias themselves possess an intrinsic self-inductance, which is represented as an equivalent inductor (L). Together, these form a parallel L–C resonant circuit at the center of the waveguide. The sections of the waveguide on either side of the central ridge can be modeled as short-circuited transmission line stubs, each with a length of $a/2$, where a is the total width of the waveguide.

The core principle of this model is that the cutoff frequency (ω_c) of the RSIW dominant mode corresponds to the resonant frequency of this entire transverse equivalent circuit. At resonance, the admittances of the central L–C tank and the two side stubs cancel each other out. This condition can be expressed by setting the total admittance at the central plane to zero:

$$Y_{LC} + Y_{stubs} = 0$$

where Y_{LC} is the admittance of the central L–C section, and Y_{stubs} is the combined admittance of the two side stubs. This leads to the resonance equation:

$$\frac{1}{\frac{1}{j\omega C} + j\omega L} - 2jY_0\cot\left(\beta_x a/2\right) = 0$$

In this equation, β_x is the propagation constant in the transverse direction. From this, β_x can be derived as:

$$\beta_x = \frac{2}{a}\cot^{-1}\left[\frac{\omega C}{2Y_0}\left(\frac{1}{1-\omega^2 LC}\right)\right]$$

The longitudinal propagation constant β for a wave traveling down the RSIW is then related to the transverse propagation constant β_x by the standard waveguide equation:

$$\beta = \sqrt{\omega^2\mu\varepsilon - \left\{\frac{2}{a}\cot^{-1}\left[\frac{\mu a h\omega^2 C}{2\pi\left(1-\omega^2 LC\right)}\right]\right\}^2}$$

Wave propagation is cut off when the longitudinal propagation constant β becomes zero. At this point, the electromagnetic wave no longer propagates along the transmission line but is confined to resonate in the cross-section. The cutoff frequency ω_c is therefore found by setting $\beta = 0$ in the above equation, which yields the following transcendental equation:

$$\omega_c\sqrt{\mu\varepsilon} = \frac{2}{a}\cot^{-1}\left(\frac{1}{2Y_0}\frac{\omega_c C}{1-\omega_c^2 LC}\right)$$
$$\theta = \frac{\pi}{2}, \beta = 0,\ Y_0 = \frac{1}{h}\sqrt{\frac{\varepsilon}{\mu}}$$

This equivalent circuit model elucidates that the ridge structure acts as a capacitive load, effectively lowering the cutoff frequency compared to a standard waveguide of the same width. This allows for a more compact physical size for a given operating band, which is a key advantage of the RSIW topology.

The proposed RSIW is realized via a standard PCB process. The stack-up consists of two layers of 0.813 mm-thick Rogers RT/duroid 4003 substrate ($\varepsilon_r = 3.55$, $\tan\delta = 0.0027$). The structure is bounded by top and bottom ground planes, which are equivalent to the top and bottom broad walls of the waveguides. Two rows of metallized via fences form the lateral walls, confining the electromagnetic field. A central ridge metal strip is patterned on the top surface of the lower substrate, and a single row of metallized vias

https://doi.org/10.1017/S1759078726103183 Published online by Cambridge University Press

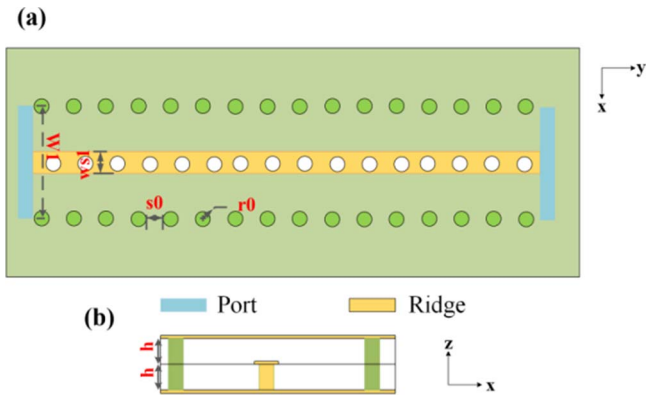


Figure 2. Schematic diagram of the RSIW configuration: (a) top view; (b) side view (dimensions: $W1 = 3.4$; $ws1 = 0.7$; $s0 = 1$; $r0 = 0.5$; $h = 0.813$ unit: mm).

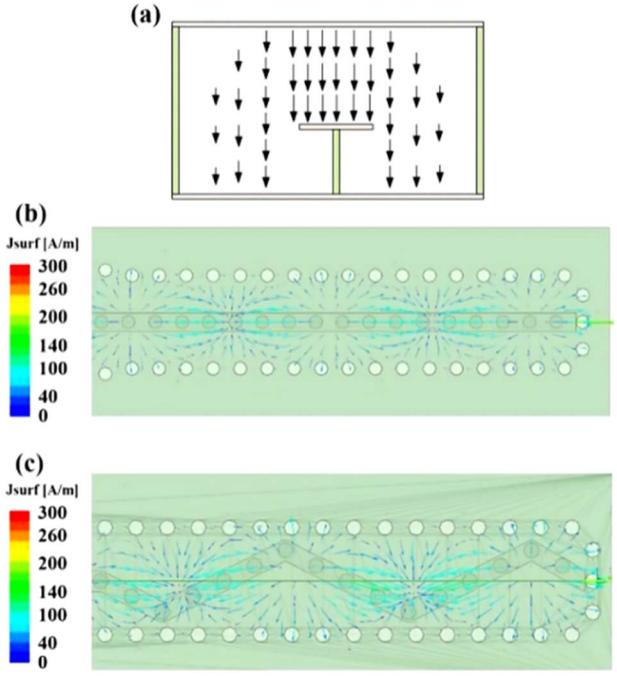


Figure 3. (a) Schematic diagram of the cross-sectional electric field of the RSIW. (b) Surface current distribution with a straight ridge. (c) Surface current distribution with a bent ridge.

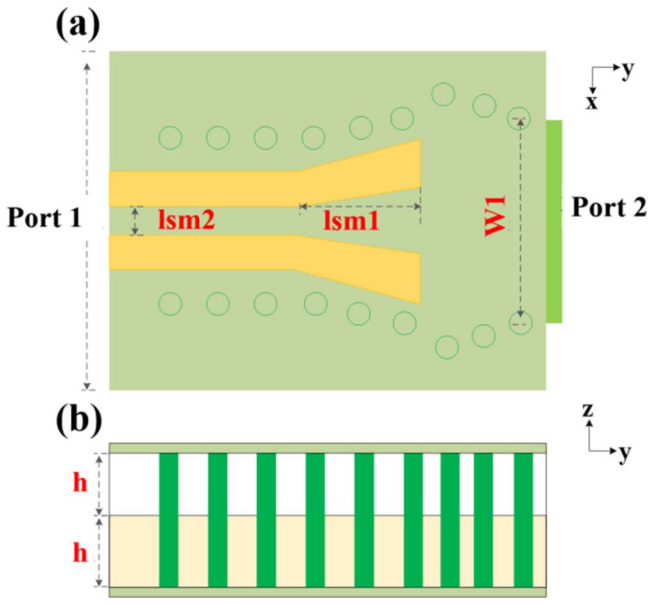


Figure 4. Schematic diagram of the grounded coplanar waveguide (GCPW)-RSIW transition: (a) top view; (b) side view (dimensions: $lsm1 = 2.5$; $lsm2 = 0.63$ unit: mm).

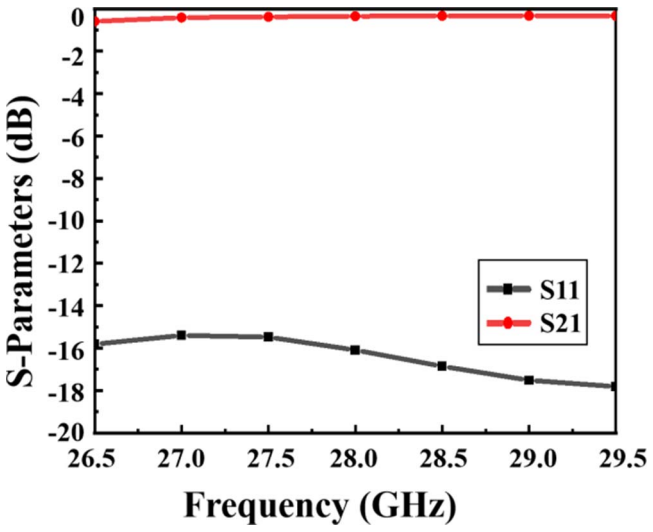


Figure 5. Simulated S-parameters of the GCPW-RSIW transition.

connects the ridge metal strip and the bottom ground plane. In this configuration, the effective height of the ridge is determined by the substrate thickness (0.813 mm), which is a constraint imposed by the standard PCB fabrication process without blind vias.

The ridge configuration is primarily responsible for adjusting the cutoff frequency and impedance characteristics of the TE_{10} mode. The initial width parameters ($W1$, $ws1$) were estimated using the analytical cutoff frequency formula for a ridge waveguide. These two parameters were optimized via the HFSS with the dual objectives of maximizing the single-mode bandwidth to cover 26.5–29.5 GHz and minimizing the insertion loss. The height ratio between the ridge and the total waveguide was set to approximately 0.5, an empirical starting point known to provide favorable impedance characteristics. The final optimized dimensions are detailed in the caption of Fig. 2.

Figure 3(a) shows the cross-sectional electric field of the RSIW, which is tightly confined above the ridge and decays rapidly toward the sidewalls. In a conventional straight-ridge RSIW (Fig. 3(b)), the longitudinal surface current is null along the centerline because of symmetry. This prevents the direct excitation of any slot placed along the centerline. By periodically bending the ridge (Fig. 3(c)), the current is forced to follow the curved path, generating a nonzero longitudinal current that reaches its maximum at the apex of each curve. When collinear slots are etched with their centers precisely aligned at the current maxima, each slot radiator is efficiently excited.

https://doi.org/10.1017/S1759078726103183 Published online by Cambridge University Press

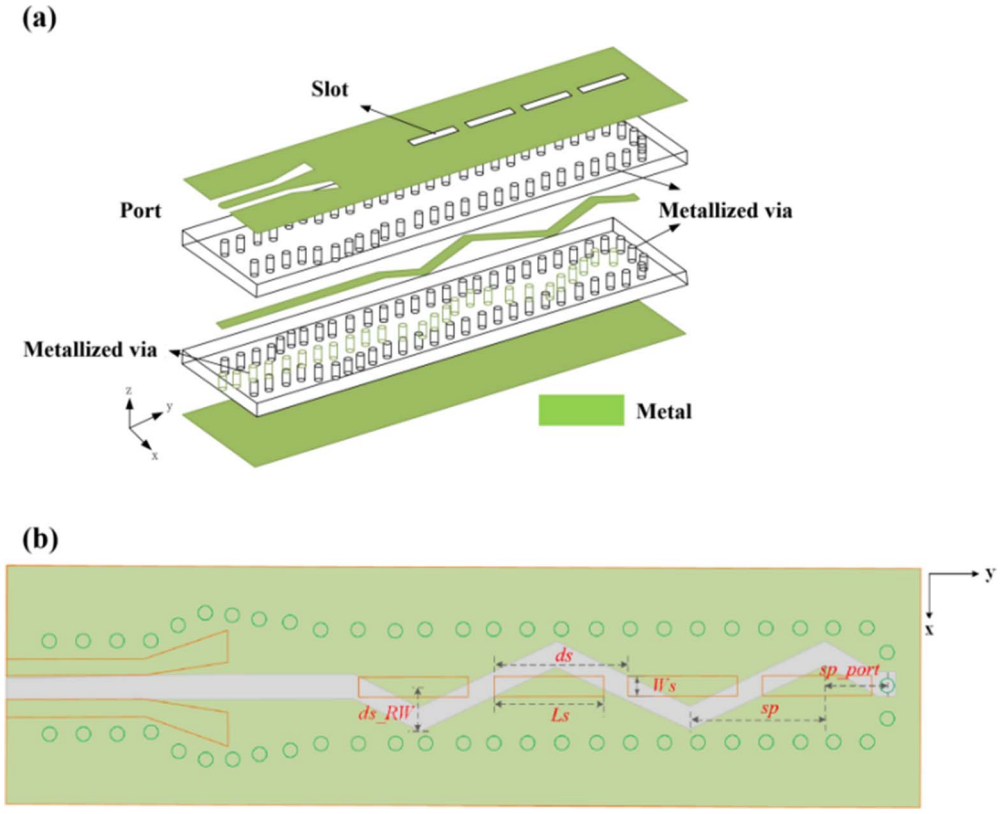


Figure 6. Schematic diagram of the collinear slot subarray: (a) exploded view; (b) top view (dimensions: *Ls* = 3.24; *Ws* = 0.63; *ds* = 3.95; sp = 2.12; *sp_port* = 1.42; *ds_RW* = 1 unit: mm).

Design of the GCPW-RSIW transition

To provide a standard 50 Ω interface for measurement and system integration, a planar GCPW-RSIW transition was codesigned on the same Rogers RT/duroid 4003 substrate. As illustrated in Fig. 4, power is coupled from the GCPW port and efficiently guided into the main RSIW section that feeds the radiating slots. After optimization for both wideband matching and low insertion loss, the final dimensions were determined (see caption of Fig. 4).

The simulated S-parameters validate the effectiveness of the design. As shown in Fig. 5, across the entire operational band, the input reflection coefficient S_{11} remains consistently below −15 dB, whereas the insertion loss S_{21} is better than 0.6 dB.

Design of the antenna subarray

The slot antenna is designed as a standing-wave, series-fed slot array. To achieve this, the waveguide is terminated with a short circuit. The first slot is positioned approximately a quarter of a guided wavelength ($\lambda_{g0}/4$) from the short-circuited end to align with a current maximum of the standing wave. Subsequent slots are spaced by approximately half a guided wavelength ($\lambda_{g0}/2$). This spacing ensures that each slot is located at a successive current maximum, leading to in-phase radiation from all elements and forming a broadside beam. The guided wavelength (λ_{g0}) at the center frequency was calculated using the standard formula:

$$\lambda_{g0} = \lambda\sqrt{1-\left(\frac{\lambda}{\lambda_c}\right)^2}$$

where λ_0 is the free-space wavelength, and λ_c is the cutoff wavelength of the designed RSIW.

As shown in Fig. 6, the subarray, which serves as the fundamental element of a larger phased array, consists of four collinear slots etched along the centerline of the ridge-bent RSIW. Each slot center is precisely aligned with the apex of the curvature, where the longitudinal surface current is maximal, ensuring efficient excitation. The transverse currents are symmetric with respect to the slot, leading to cancellation of their far-field contributions and thus low cross-polarization levels.

The choice of four radiating slots offers a good compromise between achieving sufficient element gain and maintaining a wide half-power beamwidth (HPBW), which is necessary to permit a large scan range for the assembled phased array with minimal scan loss. The subarray performance was fine-tuned through the optimization of several geometrical parameters. The slot length *Ls* primarily dictates its resonant frequency, whereas the slot width *Ws* and slot offset *ds_RW* govern the radiation strength and impedance of each slot, thereby impacting the overall impedance matching of the subarray. The final geometrical parameters are listed in the caption of Fig. 6.

As depicted in Fig. 7(a), the subarray achieves an impedance bandwidth of 26.5–29.5 GHz, corresponding to a relative bandwidth of 10.6%. The realized gain within this band is shown in Fig. 7(b), which exceeds 7.5 dBi across most frequencies. The slight gain reduction at lower frequencies is a residual effect of the series-fed topology, where minor beam squint causes the peak gain to shift slightly. Figure 8 presents the performance of the subarray at 26.75, 28, and 29.5 GHz. Examination of the *XOZ* plane (*E*-plane) radiation patterns reveals that the HPBW of the subarray is consistently

https://doi.org/10.1017/S1759078726103183 Published online by Cambridge University Press

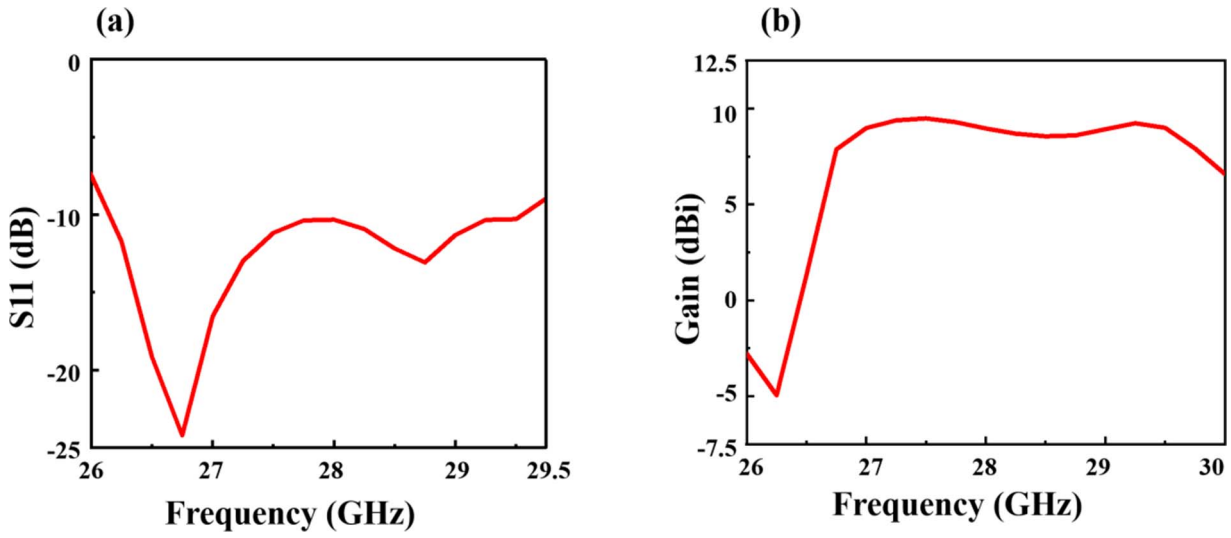


Figure 7. Simulated performance of the collinear slot subarray: (a) S_{11}; (b) gain.

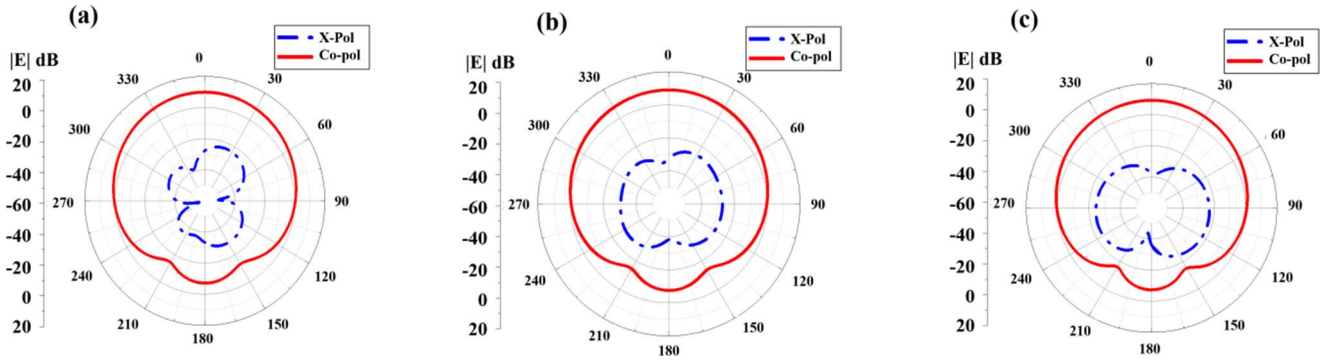


Figure 8. Simulated radiation pattern of the collinear slot subarray: (a) 26.75 GHz, (b) 28 GHz, and (c) 29.5 GHz.

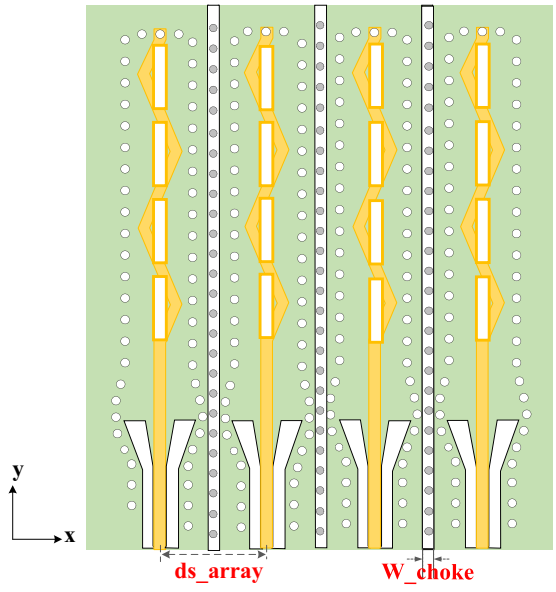


Figure 9. Schematic diagram of the 1 × 4 phased array.

above 95°. The radiation patterns exhibit excellent symmetry, and the cross-polarization level is below −20 dB in the *E*-plane.

Assembly of the phased array

The assembled 1 × 4 phased array is depicted in Fig. 9. The element spacing *ds_array* is a trade-off between two competing factors: the avoidance of grating lobes and the minimization of mutual coupling. Theoretical analysis dictates the upper limit for the spacing. To achieve a grating-lobe-free scan range of ±60°, the element spacing *ds_array* must satisfy the condition $ds_array < \lambda_0/(1 + \sin(60°))$, which is approximately $0.535\lambda_0$, where λ_0 is the free-space wavelength at the center frequency. Conversely, the lower limit is constrained by mutual coupling. An excessively small spacing leads to strong mutual coupling between elements, which can degrade impedance matching and distort the radiation patterns. To balance this trade-off, an element spacing *ds_array* of 5.3 mm was selected, which corresponds to approximately $0.5\lambda_0$ at 28 GHz.

To further mitigate the mutual coupling at this $0.5\lambda_0$ spacing and thus improve the scanning performance, a decoupling structure was integrated between the subarrays. Owing to the planar fabrication process, a conventional three-dimensional (3D) choke is impractical. Therefore, an equivalent choke structure was realized by implementing a row of periodically arranged metallized vias into the ground plane between adjacent subarrays. This structure acts as a surface wave bandgap, suppressing unwanted

https://doi.org/10.1017/S1759078726103183 Published online by Cambridge University Press

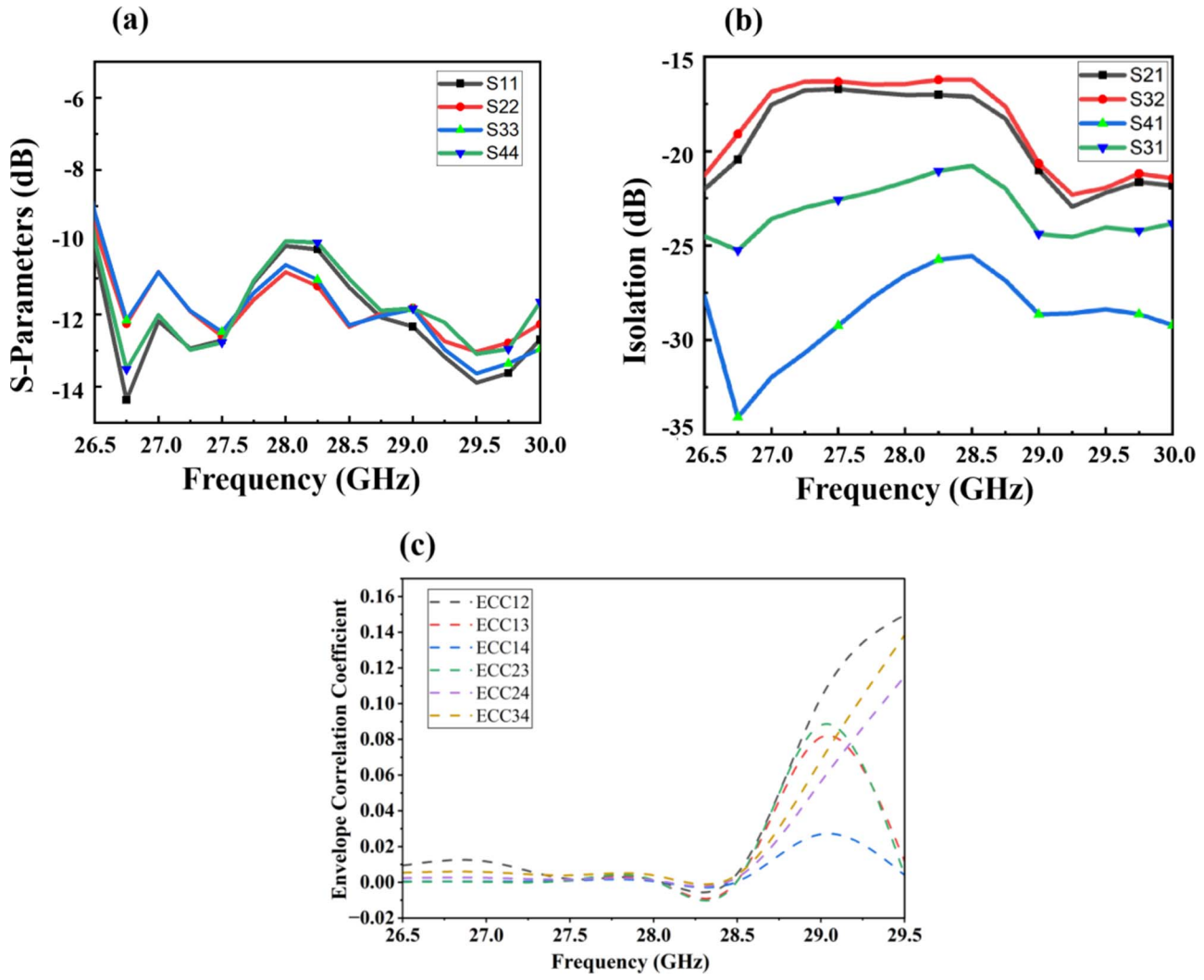


Figure 10. Simulated performance of the 1 × 4 phased array: (a) reflection coefficient, (b) port isolation, and (c) envelope correlation coefficient.

propagation between subarrays. The width of this choke *W_choke* is set to 0.5 mm, and the overall dimensions of the array antenna are $2.15 \times 2.5 \times 0.17\lambda_0$ @28 GHz.

To achieve electronically controlled 1D scanning, the array is excited by four feed ports with equal amplitudes. A progressive phase shift is applied between adjacent subarrays, which steers the main beam. As illustrated in Fig. 10(a), the reflection coefficient S_{11} remains below −10 dB across the 26.5–29.5 GHz band, corresponding to a 10.7% bandwidth and covering the 5G n257 band. The simulations of the transmission coefficients, shown in Fig. 10(b), reveal that the isolation between adjacent ports (1–2, 2–3, 3–1, and 4–1) is better than −16 dB across the band. The envelope correlation coefficient (ECC) was evaluated using embedded element far-field patterns, as shown in Fig. 10(c). Within 26.5–28.5 GHz, all ECC values remain below 0.01, indicating excellent port isolation and radiation pattern diversity. A noticeable increase in ECC is observed above 29 GHz, suggesting degradation near the upper band edge.

As depicted in Fig. 11, the array's broadside realized gain is 13.2 dBi at 26.75 GHz and increases to 14.77 dBi at 29.5 GHz. The radiation efficiency, accounting for metal and dielectric losses, exceeds 70% across most of the operating band.

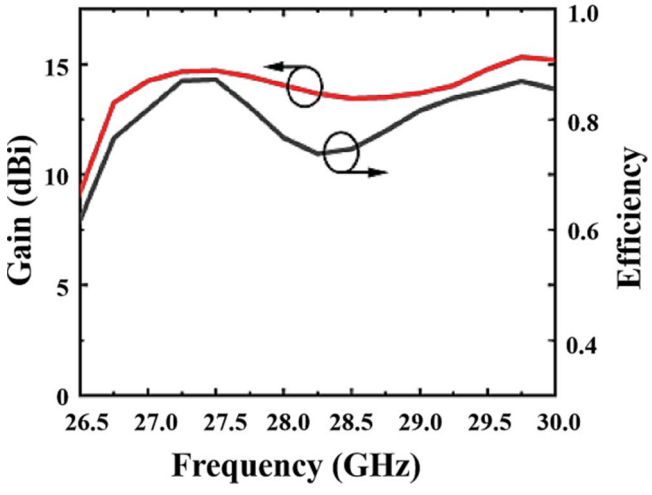


Figure 11. Simulated gain and efficiency of the 1 × 4 phased array.

The scanning performances of the 1 × 4 array at 26.75, 28, and 29.5 GHz are presented in Fig. 12. The gain decreases smoothly

https://doi.org/10.1017/S1759078726103183 Published online by Cambridge University Press

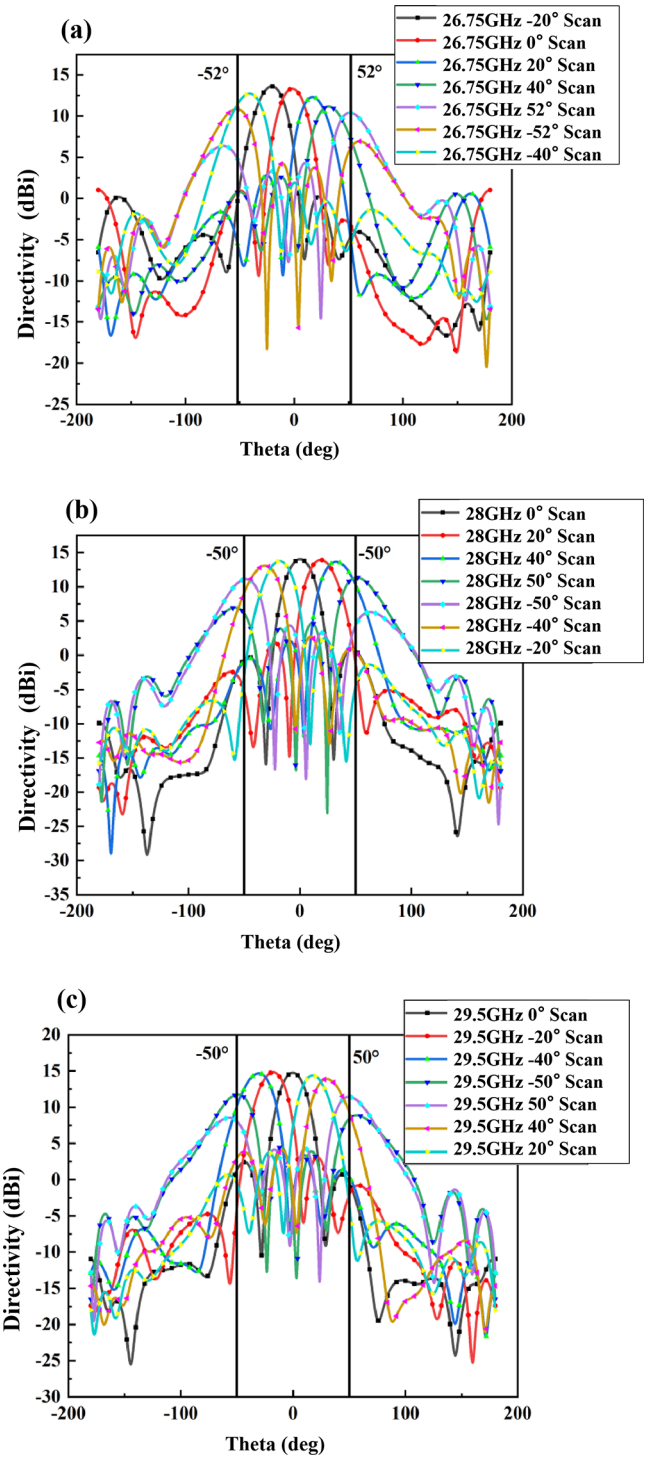


Figure 12. Simulated directivity of a 1 × 4 phased array: (a) *E*-plane scan at 26.75 GHz; (b) *E*-plane scan at 28 GHz; and (c) *E*-plane scan at 29.5 GHz.

as the beam is steered away from the broadside. Specifically, at 28 GHz, 3-dB gain roll-off occurs at a scan angle of ±50°. At the band edges (26.75 and 29.5 GHz), the scan ranges for a 3-dB gain roll-off are ±52° and ±50°, respectively, demonstrating wide-angle scanning capability across the entire operational bandwidth.

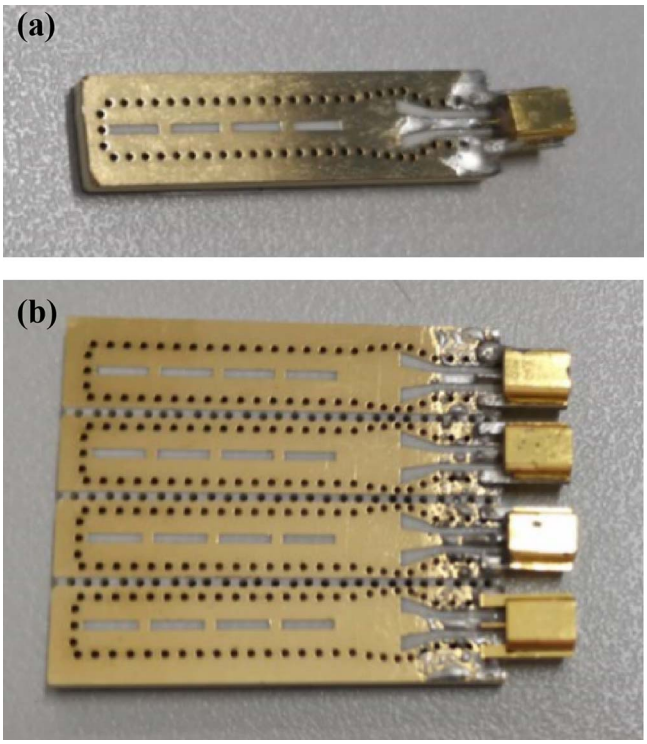


Figure 13. Fabricated prototypes of the (a) subarray and (b) 1 × 4 phased array.

Measurement and performance comparison

To validate the performance of the proposed collinear slot phased array, a prototype was fabricated using a Rogers RT/duroid 4003 dielectric substrate with a single-layer thickness of 0.813 mm. The array features a simple structure, with all the elements integrated on two dielectric substrates, which were bonded together via the RO4450F adhesive. The fabrication process relies solely on PCB technology, offering significant cost advantages. A photo of the fabricated prototype is shown in Fig. 13.

The ports of the 1 × 4 array were securely mounted to 2.92 mm connectors with a characteristic impedance of 50 Ω. The matching and radiation characteristics of the antenna were assessed via a vector network analyzer (R&S ZVA67 VNA) and an MVG Satimo StarLab microwave chamber. Given that the element spacing for the BBOX BB-ONE-JF-28- digital phase shifter (4 × 4/8 × 8) is ∼5 mm, the antenna was directly connected to the phase shifter during testing, as shown in Fig. 14. Notably, owing to a mounting flange on the chamber turntable that obstructed the rear hemisphere, only the forward radiation performance (from −90° to +90°) could be reliably measured.

The measured S-parameters and radiation characteristics of the fabricated subarray prototype were compared against the simulation results. Figure 15 presents a comparison of the measured and simulated reflection coefficients S_{11}. The measured S_{11} shows good agreement with the simulation across the majority of the target frequency band. A deviation is observed at the lower band edge, where the measured S_{11} is slightly above −10 dB. This discrepancy is attributed primarily to the impedance mismatch introduced by the solder transition between the 2.92 mm connector and the feed port of the antenna, which is a common factor for prototypes at these frequencies. Minor fabrication tolerances may also be a contributing factor.

https://doi.org/10.1017/S1759078726103183 Published online by Cambridge University Press

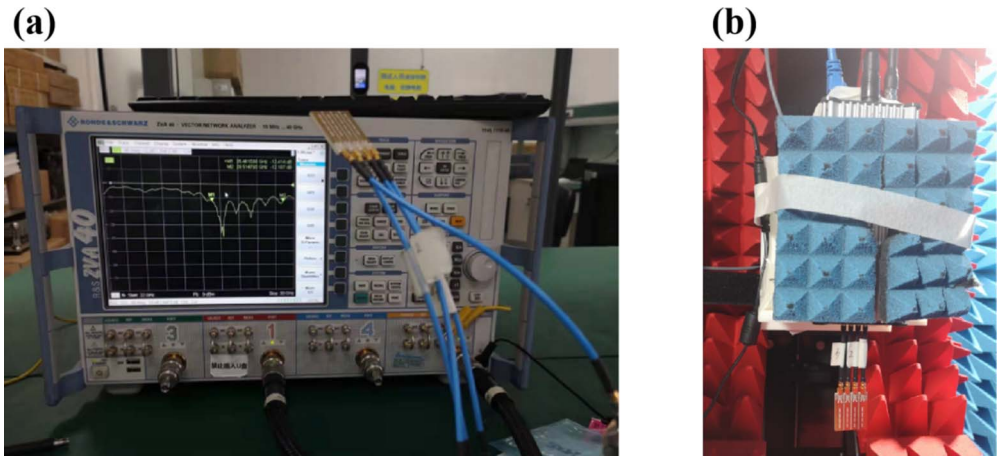


Figure 14. Measurement setup for (a) S-parameter and (b) gain.

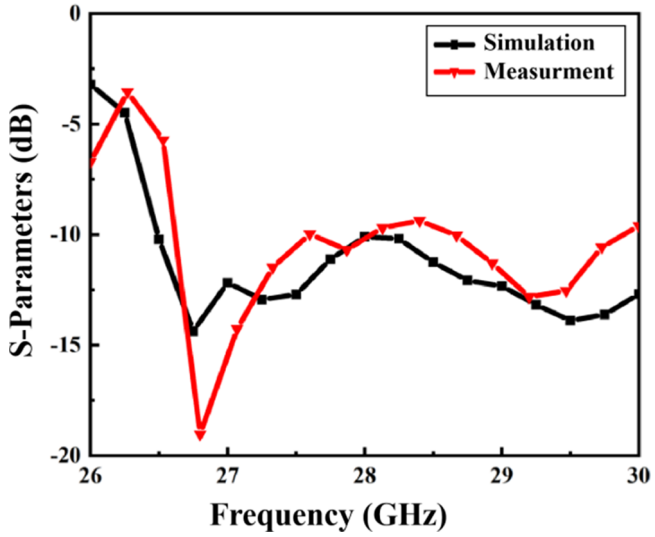


Figure 15. Simulated and measured S_{11} of the subarray.

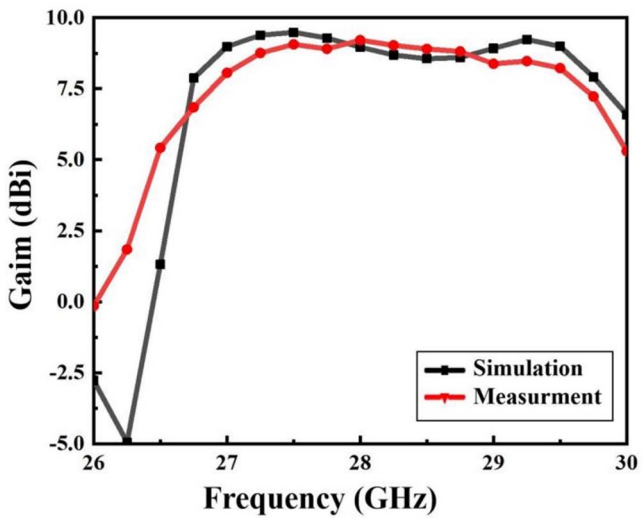


Figure 16. Simulated and measured gains of the subarray.

The measured and simulated realized gains are compared in Fig. 16. The measurement results confirm a stable gain profile across the frequency band. The measured gain tracks the simulated curve closely, with a maximum deviation of less than 1 dB observed at the lower band edge. This level of agreement is well within acceptable margins and validates the subarray performance.

Figure 17 shows a comparison of the normalized radiation patterns in the *XOZ*-plane (*E*-plane) at 26.75, 28, and 29.5 GHz. Excellent agreement is observed between the measured and simulated patterns. Key features such as the main lobe shape and the HPBW are accurately reproduced in the measurement. The minor discrepancies in side-lobe levels can be attributed to the test environment and manufacturing tolerances.

The fabricated 1 × 4 phased array prototype was measured and compared against the simulation results to validate its performance. The four ports are driven simultaneously with equal amplitudes and controlled phase shifts to synthesize a single beam for electronic steering instead of transmitting independent data streams from uncorrelated ports. Figure 18 compares the measured and simulated reflection coefficients S_{11} for the center port of the array. The measured results show a similar resonant performance to those of the simulation, and the measured −10 dB impedance bandwidth successfully covers the target n257 band (26.5–29.5 GHz). The slight frequency shift and greater reflection at the band edges are attributed primarily to fabrication tolerances and the impedance mismatch introduced by the manual soldering of the 2.92 mm connectors. The port isolation is evaluated by the transmission coefficient S_{21} between adjacent subarrays, as shown in Fig. 19. The measured isolation is better than 19 dB across the band. The measured and simulated broadside realized gains are presented in Fig. 20. The measured gain exceeds 12 dBi across most of the band, peaking at 14.5 dBi. A discrepancy of 1–2 dB is observed between the measurements and simulations. This gain reduction can be attributed to insertion loss from the 2.92 mm connectors and solder transitions (estimated at ∼0.5 dB per connector).

The measured scanning patterns in the *E*-plane are shown in Fig. 21. At 28 GHz, the measured 3-dB scan range is ±45°, which closely matches the simulated performance. At 29.5 GHz, however, the measured 3-dB scan range is asymmetrical, ranging from −45° to +55°. This asymmetry, resulting in an apparent 5° shift in the positive scan direction, strongly suggests the presence of

https://doi.org/10.1017/S1759078726103183 Published online by Cambridge University Press

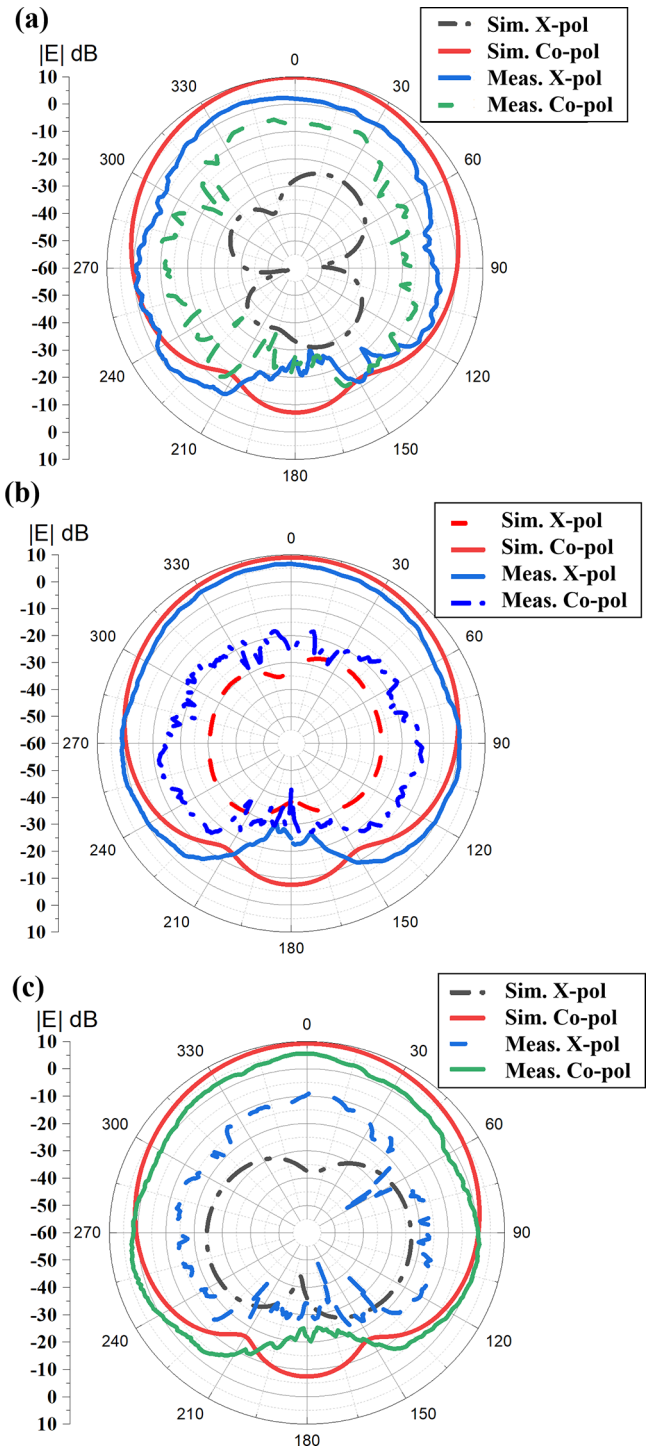


Figure 17. Normalized radiation patterns of the subarray at (a) 26.75 GHz, (b) 28 GHz, and (c) 29.5 GHz.

asystematic phase error in the test setup. This could originate from unequal cable lengths or minor calibration inaccuracies in the digital phase shifter, which introduces a progressive phase error that becomes more pronounced as the beam is steered.

Despite the identified discrepancies, the measurement results effectively validate the proposed design. The fabricated array demonstrates the required impedance bandwidth, high port isolation, and wide-angle scanning capability.

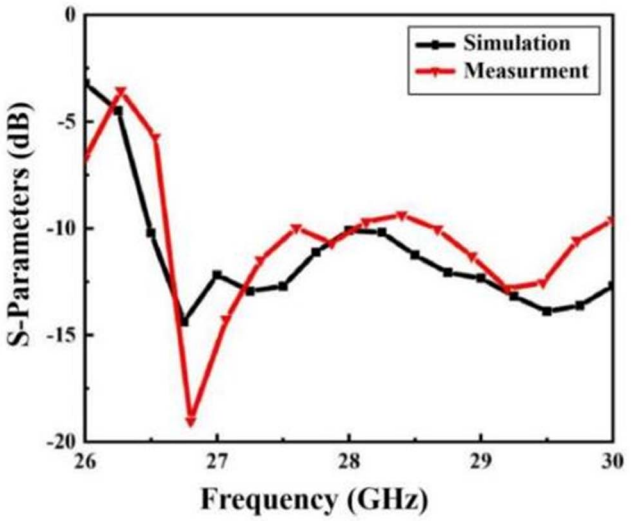


Figure 18. Simulated and measured S_{11} for the 1 × 4 phased array.

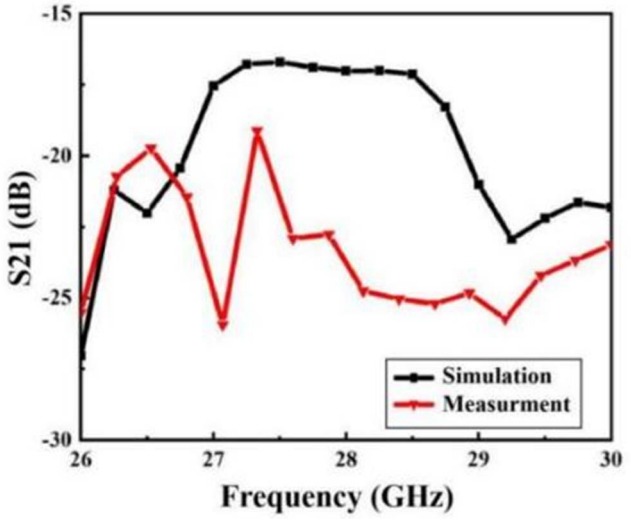


Figure 19. Simulated and measured port isolation for the 1 × 4 phased array.

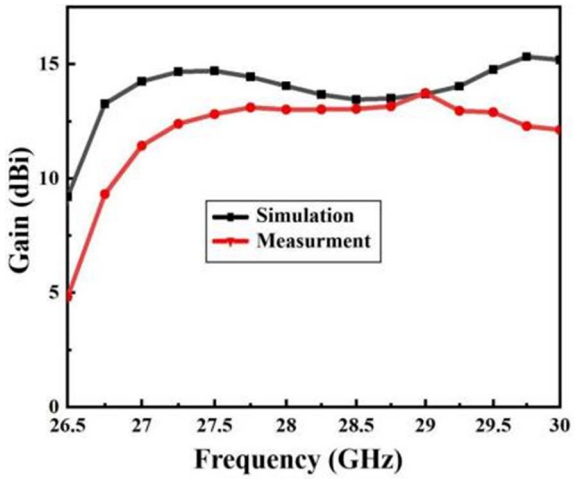


Figure 20. Simulated and measured gains for the 1 × 4 phased array.

https://doi.org/10.1017/S1759078726103183 Published online by Cambridge University Press

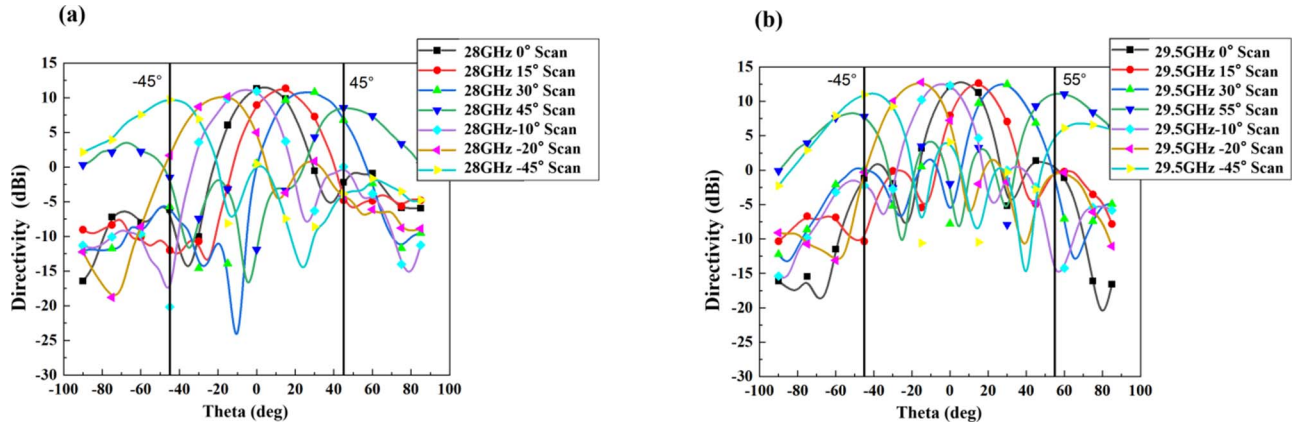


Figure 21. Measured scanning patterns of the 1 × 4 phased array: (a) 28 GHz; (b) 29.5 GHz.

Table 1. Comparison of various antenna arrays

Refs.	Configuration	3-dB scanning (°)	Working frequency		Peak gain (dBi)	Isolation (dB)	No. of elements	Size ($\lambda_0 \times \lambda_0$)
			GHz	BW (%)				
[23]	Slotted SIW	±34	24.0–29.5	20.85	9.27	16.3	4	3.32 × 1.80
[24]	Slotted SIW	±42	25.03–28.96	14.6	9.7	18	4	2.65 × 1.48
[25]	Slotted SIW	±41	25.8–28.8	11	10.2	15.5	4	2.13 × 1.82
[26]	SIW	±60	28	N/A	9.2	20	16	9.21 × 13.39
[27]	Vivaldi	N/A	11.5–21.3	59.76	10.6	25	2	2.73 × 2.73
[28]	Patch	N/A	24–32	28.6	5.8	20	4	4.48 × 1.12
[29]	Patch	N/A	27–30/35.54–41	10.5/14.2	7.5	25	4	5.70 × 5.70
[30]	T-slot	N/A	3.37–3.61/4.9–5.1	6.9/4	3.9	14	8	1.74 × 0.87
[31]	Tri-circular ring	N/A	26–40	42.4	6.6	18	4	3.08 × 3.08
[32]	DPST and DGST	N/A	24–34	34.5	6.4	21	4	2.42 × 0.97
This work	Slotted RSIW	±50	26.5–29.5	10.7	14.5	19	4	2.15 × 2.50

To benchmark the performance of the proposed array, a comparison with other state-of-the-art SIW-based scanning arrays is presented in Table 1. In terms of the scanning range, the proposed array achieves a wide 3-dB scan range of over ±50°. This range is significantly wider than the ±34°, ±42°, and ±41° scanning ranges of the 4-element arrays reported in Li et al., Zhu and Deng, and Liu and Yan [23–25]. While the 16-element array in Puskely et al. [26] reported wider ranges, our design demonstrated highly competitive wide-angle scanning capability via a simple 1 × 4 configuration. The proposed array achieves a peak gain of 14.5 dBi, which is substantially greater than that of all the compared 4-element arrays, whose gains are between 9.27 and 10.2 dBi. Crucially, our 4-element array even surpasses the gain of the 16-element array in Puskely et al. [26] by more than 5.5 dB, highlighting the high radiation efficiency of the collinear slot element. Furthermore, the proposed design results in excellent port isolation. The measured isolation is better than 19 dB, which is superior to that of Li et al., Zhu and Deng, and Liu and Yan [23–25] and is comparable to the high isolation achieved in Puskely et al. [26].

To provide a broader context, we also compare our work with several recently published high-performance multiple-input multiple-output (MIMO) antennas [27–32]. It is important to recognize that these antennas are primarily designed for spatial diversity and multiplexing, prioritizing wide bandwidth and high isolation between low-gain elements. These MIMO designs often achieve impressive bandwidths (e.g., 59.76% in Wang et al. [27]) and excellent isolation (e.g., 25 dB in Wang et al. and Sethi et al. [27, 29]). However, these strengths come at the cost of a lower peak gain, which is typically below 11 dBi. Crucially, as their primary function is not beamforming, a beam-scanning range is not a key figure-of-merit for these designs. Our proposed phased array achieves a peak gain of 14.5 dBi and a wide scanning range of ±50°, demonstrating its advantage and suitability for high-gain directional beamforming applications required to overcome significant path loss in mmWave communication.

Conclusion

In this paper, a low-cost, high-performance 1 × 4 collinear slot phased array for 5G mmWave applications is proposed. The design introduces a periodically bending ridge in an RSIW to enable an efficient low-cross-polarization centerline collinear slot radiator.

https://doi.org/10.1017/S1759078726103183 Published online by Cambridge University Press

Furthermore, an integrated via-based choke structure is also introduced for effective mutual coupling suppression. The fabricated prototype, built on a standard two-layer PCB process, successfully operates over the 26.5–29.5 GHz band (10.7% bandwidth). The measurement results demonstrate a peak gain of 14.5 dBi, inter-element isolation better than 19 dB, and a wide 3-dB scanning range of ±50°. The demonstrated performance makes this 1 × 4 array a practical solution for applications requiring a balance of gain and compact size, such as 5G customer devices and Vehicle-to-Everything (V2X) systems. Furthermore, this work validates the proposed architecture, confirming its suitability as a scalable unit for constructing larger arrays (e.g., 4 × 4 or 8 × 8) to meet higher-gain requirements.

Funding statement. This study was supported in part by the National Natural Science Foundation of China under Grant 62371141 and in part by the Guangzhou Basic and Applied Basic Research Scheme (2025A04J5283).

Competing interests. The authors declare that they have no known competing financial interests or personal relationships that could have appeared to influence the work reported in this paper.

References

1. **Pant M and Malviya L** (2022) Design, developments, and applications of 5G antennas: A review. *International Journal of Microwave and Wireless Technologies* **15**(1), 156–182. https://doi.org/10.1017/s1759078722000095
2. **Nahar T and Rawat S** (2021) Survey of various bandwidth enhancement techniques used for 5G antennas. *International Journal of Microwave and Wireless Technologies* **14**(2), 204–224. https://doi.org/10.1017/s1759078720001804
3. **Andrews JG Buzzi S, Choi W, Hanly SV, Lozano A, Soong AC, Zhang JC** (2014) What will 5G be? *IEEE Journal on Selected Areas in Communications* **32**(6), 1065–1082. https://doi.org/10.1109/JSAC.2014.2328098
4. **Qu Z, Qu S-W, Zhang Z, Yang S and Chan CH** (2020) Wide-angle scanning lens fed by small-scale antenna array for 5G in millimeter-wave band. *IEEE Transactions on Antennas and Propagation* **68**(5), 3635–3643. https://doi.org/10.1109/TAP.2020.2967086
5. **Xu S, Jin G, Lu D and Liao S** (2025) Millimeter-wave wideband high-gain LTCC phased array antenna based on ridged substrate integrated waveguide. *International Journal of Microwave and Wireless Technologies* **17**(4), 642–652. https://doi.org/10.1017/s1759078725000534
6. **Chung M-A, Lee M-C, Hsu -C-C and Lin C-W** (2024) Beamforming steering implementation using substrate-integrated waveguide Butler matrix and slotted array antenna for 5G n257 band. *International Journal of Microwave and Wireless Technologies* **16**(8), 1381–1396. https://doi.org/10.1017/s1759078724001284
7. **Yang G, Li J, Zhou SG and Qi Y** (2017) A wide-angle E-plane scanning linear array antenna with wide beam elements. *IEEE Antennas and Wireless Propagation Letters* **16**, 2923–2926. https://doi.org/10.1109/LAWP.2017.2752713
8. **Yang G, Zhang Y and Zhang S** (2021) Wide-band and wide-angle scanning phased array antenna for mobile communication system. *IEEE Open Journal of Antennas and Propagation* **2**, 203–212. https://doi.org/10.1109/OJAP.2021.3057062
9. **Cheng YF, Ding X, Shao W and Wang B-Z** (2017) Planar wide-angle scanning phased array with pattern-reconfigurable windmill-shaped loop elements. *IEEE Transactions on Antennas and Propagation* **65**(2), 932–936. https://doi.org/10.1109/TAP.2016.2632736
10. **Elobied AA, Yang XX, Lou T and Gao S** (2021) Compact 2 × 2 MIMO antenna with low mutual coupling based on half mode substrate integrated waveguide. *IEEE Transactions on Antennas and Propagation* **69**(5), 2975–2980. https://doi.org/10.1109/TAP.2020.3028250
11. **Yang H, Cao X, Gao J, Yang H and Li T** (2020) A wide-beam antenna for wide-angle scanning linear phased arrays. *IEEE Antennas and Wireless Propagation Letters* **19**(12), 2122–2126. https://doi.org/10.1109/LAWP.2020.3024617
12. **Feng Y Li JY, Zhang LK, Yu XJ, Qi YX, Li D and Zhou SG** (2022) A broadband wide-angle scanning linear array antenna with suppressed mutual coupling for 5G sub-6G applications. *IEEE Antennas and Wireless Propagation Letters* **21**(2), 366–370. https://doi.org/10.1109/LAWP.2021.3131806
13. **Wang Z, Tu Z-H, Yuan Z and Chen F-C** (2023) Decoupling and wide-angle scanning design of a millimeter-wave phased array using square-ring metasurface. *IEEE Antennas and Wireless Propagation Letters* **22**(8), 1828–1832. https://doi.org/10.1109/LAWP.2023.3266266
14. **Li Y and Xiao S** (2022) Wideband wide-angle scanning phased array based on miniaturized metasurface antenna. *IEEE Transactions on Antennas and Propagation* **70**(2), 1107–1119. https://doi.org/10.1109/TAP.2021.3111301
15. **Fan X and Wang Y** (2023) Compact millimeter-wave array with wide-angle scanning for mobile phones. *IEEE Transactions on Antennas and Propagation* **71**(8), 6983–6988. https://doi.org/10.1109/TAP.2023.3278872
16. **Jin G, Sun Y, Liao S, Wang QXJ, Cao Y, Che W and Xue Q** (2024) Wide-angle beam-scanning millimeter-wave antenna array using phase-controlled beam-steerable elements. *IEEE Transactions on Antennas and Propagation* **72**(4), 3730–3735. https://doi.org/10.1109/TAP.2024.3361510
17. **Moscato S, Moro R, Pasian M, Bozzi M and Perregrini L** (2015) Two-material ridge substrate integrated waveguide for ultra-wideband applications. *IEEE Transactions on Microwave Theory and Techniques* **63**(10), 3175–3182. https://doi.org/10.1109/tmtt.2015.2461612
18. **Kazemi R and Fathy AE** (2014) UWB 4-element ridge-SIW vivaldi antenna array. In *2014 IEEE Antennas and Propagation Society International Symposium (APSURSI)*, Memphis, TN, USA, July 2014. IEEE, pp. 1039–1040. https://doi.org/10.1109/aps.2014.6904846
19. **Ding Y and Wu K** (2009) A 4×4 ridge substrate integrated waveguide (RSIW) Slot array antenna. *IEEE Antennas and Wireless Propagation Letters* **8**, 561–564. https://doi.org/10.1109/lawp.2009.2021006
20. **Wang W, Zhong S-S, Zhang YM and Liang XL** (2006) A broadband slotted ridge waveguide antenna array. *IEEE Transactions on Antennas and Propagation* **54**(8), 2416–2420. https://doi.org/10.1109/TAP.2006.879216
21. **Mallahzadeh A and Mohammad-Ali-Nezhad S** (2015) A low cross-polarization slotted ridged SIW array antenna design with mutual coupling considerations. *IEEE Transactions on Antennas and Propagation* **63**(10), 4324–4333. https://doi.org/10.1109/TAP.2015.2457952
22. **Wei B, Li Z, Wang S, Liu S, Li S and Wang J** (2023) Ku/Ka dual-band shared-aperture leaky-wave antenna with fixed-frequency and wide-angle beam scanning based on ridged SIW. *IEEE Transactions on Antennas and Propagation* **71**(5), 4558–4563. https://doi.org/10.1109/TAP.2023.3240823
23. **Li H, Li Y, Chang L, Sun W, Qin X and Wang H** (2021) A wide-band dual-polarized endfire antenna array with overlapped apertures and small clearance for 5G millimeter-wave applications. *IEEE Transactions on Antennas and Propagation* **69**(2), 815–824. https://doi.org/10.1109/TAP.2020.3016512
24. **Zhu Y and Deng C** (2023) Wideband dual-polarized endfire phased array antenna with small ground clearance for 5G mmWave mobile terminals. *IEEE Transactions on Antennas and Propagation* **71**(6), 5469–5474. https://doi.org/10.1109/TAP.2023.3263007
25. **Liu W and Yan S** (2022) A design of millimeter-wave dual-polarized SIW phased array antenna using characteristic mode analysis. *IEEE Antennas and Wireless Propagation Letters* **21**(1), 29–33. https://doi.org/10.1109/LAWP.2021.3116260
26. **Puskely J, Mikulasek T, Aslan Y, Roederer A and Yarovoy A** (2022) 5G SIW-based phased antenna array with cosecant-squared shaped pattern. *IEEE Transactions on Antennas and Propagation* **70**(1), 250–259. https://doi.org/10.1109/TAP.2021.3098577
27. **Wang W Fang Z, Tang K, Wang X, Shu Z, Zhao Z and Zheng Y** (2023) Wideband gain enhancement of MIMO antenna and its application in FMCW radar sensor integrated with CMOS-based transceiver chip for human respiratory monitoring. *IEEE Transactions on Antennas and Propagation* **71**(1), 318–329. https://doi.org/10.1109/tap.2022.3222802
28. **Munir ME, Nasralla MM and Farman H** (2024) Design and development of super-compact millimeter wave antenna for future 5G vehicular applications, In *2024 IEEE 100th Vehicular Technology Conference (VTC2024-Fall)*, Washington, DC, USA, Oct. 2024, IEEE, October, pp. 1–8. https://doi.org/10.1109/vtc2024-fall63153.2024.10757480

29. **Sethi WT, Kiani SH, Munir ME, Sehrai DA, Şerif Savci H and Awan D** (2024) Pattern diversity based four-element dual-band MIMO patch antenna for 5G mmWave communication networks. *Journal of Infrared, Millimeter, and Terahertz Waves* **45**(5–6), 521–537. https://doi.org/10.1007/s10762-024-00983-0
30. **Abubakar HS Zhao Z, Munir ME, Tareen WU, Wang B, Kiani SH, Ali T** (2024) Enhanced smartphone connectivity: Dual-band MIMO antenna with high isolation and low ECC. *Physica Scripta* **99**(6), 065524. https://doi.org/10.1088/1402-4896/ad4424
31. **Nasralla MM, Munir ME, Farman H and Choudhury N** (2025) Design and analysis of millimeter-wave antenna for new radio (NR) 5G bands supporting a green wireless future. *Wireless World Research and Trends Magazine*, 9–14. https://doi.org/10.13052/2794-7254.015
32. **Munir ME, Nasralla MM and Esmail MA** (2025) Design and analysis of 8×1 wideband mmwave MIMO antenna array for high-performance 5G UAV communications. In *2025 IEEE 101st Vehicular Technology Conference (VTC2025-Spring)*, Prague, Czech Republic, May 2025 IEEE, pp. 1–7. https://doi.org/10.1109/vtc2025-spring65109.2025.11174691

https://doi.org/10.1017/S1759078726103183 Published online by Cambridge University Press